condensed matter

MDPI

Article

Fe_3O_4@SiO_2-NH_2 Functionalized Nanoparticles as a Potential Contrast Agent in Magnetic Resonance

Brayan Stick Betin Bohorquez [1], Indry Milena Saavedra Gaona [2], Carlos Arturo Parra Vargas [2], Karina Vargas-Sánchez [3], Jahaziel Amaya [1], Mónica Losada-Barragán [4], Javier Rincón [1] and Daniel Llamosa Pérez [1,*]

1 Grupo de Investigación Fundamental y Aplicada en Materiales GIFAM, Facultad de Ciencias, Universidad Antonio Nariño, Cra. 1 este #47a15, Bogotá 110231, Colombia; bbetin96@uan.edu.co (B.S.B.B.); jamaya47@uan.edu.co (J.A.); rolrincon@uan.edu.co (J.R.)
2 Grupo Física de Materiales, Escuela de Física, Universidad Pedagógica y Tecnológica de Colombia, Av. Central del Norte #39-115, Tunja 150003, Boyacá, Colombia; indry.saavedra@uptc.edu.co (I.M.S.G.); carlos.parra@uptc.edu.co (C.A.P.V.)
3 Laboratorio de Neurofisiología Celular, Grupo de Neurociencia Traslacional, Facultad de Medicina, Universidad de los Andes, Bogotá 111711, Colombia; j.vargass@uniandes.edu.co
4 Grupo de Biología Celular y Funcional e Ingeniería de Biomoleculas, Facultad de Ciencias, Universidad Antonio Nariño, Cra. 1 este #47a15, Bogotá 110231, Colombia; monica.losada@uan.edu.co
* Correspondence: dllamosa@uan.edu.co

Abstract: The present work proposes a method for the synthesis of a nanoparticle with a superparamagnetic Fe_3O_4 core coated with SiO_2-NH_2 by ultrasound-assisted coprecipitation. Additionally, the nanoparticle is functionalized with a microinflammation biomarker peptide, and its effects on the viability of monkey kidney endothelial cells and the Vero cell line were evaluated. The main physicochemical properties of the nanoparticles were characterized by X-ray diffraction (XRD), Fourier transform infrared spectroscopy (FTIR), thermogravimetric analysis (TGA), a vibrating sample magnetometer (VSM), a field emission scanning electron, Scanning Electron Microscopy (SEM), and High-Resolution Transmission Electron Microscopy (HR-TEM). The results showed that the nanoparticles are spherical, with sizes smaller than 10 nm, with high thermal stability and superparamagnetic properties. They also demonstrated cell viability rates exceeding 85% through Magnetic Resonance Imaging (MRI). The results indicate the potential of these nanoparticles to be used as a contrast agent in magnetic resonance to detect mild brain lesions.

Keywords: nanoparticles; Fe_3O_4; contrast agent; ultrasound-assisted synthesis; biomarkers; superparamagnetic

Citation: Betin Bohorquez, B.S.; Saavedra Gaona, I.M.; Parra Vargas, C.A.; Vargas-Sánchez, K.; Amaya, J.; Losada-Barragán, M.; Rincón, J.; Llamosa Pérez, D. Fe_3O_4@SiO_2-NH_2 Functionalized Nanoparticles as a Potential Contrast Agent in Magnetic Resonance. *Condens. Matter* **2024**, *9*, 49. https://doi.org/10.3390/condmat9040049

Academic Editor: Víctor Manuel García Suárez

Received: 8 October 2024
Revised: 8 November 2024
Accepted: 13 November 2024
Published: 17 November 2024

1. Introduction

The blood–brain barrier (BBB) is a dynamic, semi-permeable, and functional platform that separates and regulates the interaction between the blood system and the central nervous system (CNS), allowing blood to flow freely to the brain but preventing the interaction between transported foreign substances by the bloodstream and brain cells [1,2]. Therefore, the BBB plays an essential role in metabolism, defense against pathogens and toxins, and neuronal interaction, among other functions [3,4]. The BBB comprises different brain cells, such as pericytes, astrocytes, and endothelial cells (EC), which work together to keep the neural environment intact [5–7]. This cell nucleus also directly interacts with microglia and specific neurons [8,9].

It is important to highlight that various mechanisms regulate the passage of vital substances or waste products between the brain and the bloodstream [10,11]. These included passive diffusion, which allows lipophilic molecules weighing less than 400 Da to cross; specific transporters that facilitate the movement of small hydrophilic molecules like

glucose and amino acids; and receptors that enable the endocytosis of large molecules, such as insulin [12]. However, the proper function of the BBB can be compromised by traumatic brain injuries (TBI), which result from blows or falls that impact the head [13,14]. Such dysfunctions, in turn, may contribute to the development of neurodegenerative diseases, including Alzheimer's disease, multiple sclerosis, Parkinson's disease, and Huntington's disease. In severe cases, TBIs can also lead to coma and subsequent death [15,16].

TBIs are classified based on the extent of damage, ranging from mild to severe, with severe TBIs potentially being life-threatening [17]. It is important to note that mild TBIs can cause persistent symptoms such as acute headaches, impaired cognitive function, fatigue, significant damage to brain cells (including those of the BBB), and consequent changes in brain chemistry [18]. If not treated correctly, mild TBIs can progress into more severe injuries, disrupting brain metabolism and increasing the risk of neurodegenerative diseases or death [19,20].

Novel brain imaging techniques have been developed, including an electroencephalogram (EEG), computed tomography (CT), magnetic resonance imaging (MRI), and functional magnetic resonance imaging (FMRI) [21]. Although FMRI can detect mild TBIs, it is an expensive and complex technique with limited availability in hospitals [22]. As a result, there is a global effort to improve the resolution of more affordable imaging methods, such as MRI, to reduce costs while enabling accurate and timely detection of mild TBIs [23]. Therefore, contrast agents that significantly improve image quality have been proposed [24], particularly those with magnetic properties, such as gadolinium and iron oxides [25]. However, these agents need more specificity when identifying TBIs [26].

Current approaches focus on developing magnetic nanoparticles as contrast agents capable of crossing biological barriers due to their small size without disrupting the body's homeostasis [27]. The most commonly reported nanoparticles for MRI are those with superparamagnetic properties, which generate magnetic ordering in the presence of a magnetic field [26,28]. Among these, the most studied are Fe_3O_4 nanoparticles, with sizes less than 30 nm, due to their stability and physical properties [29]. These nanoparticles enhance MRI resolution by shortening T2/T2* relaxation times, derived from their superparamagnetic properties [30]. Additionally, it has been reported that these nanoparticles, with the proper morphology and size, can pass through the BBB, offering the potential for detecting CNS damage [31]. Many synthesis routes exist to obtain Fe_3O_4 nanoparticles with the desired characteristics [32]. Since the used precursors have affordable prices and are of low ecological risk, the most commonly used techniques are chemical coprecipitation from iron salts (sulfates or chlorides) and the use of strong bases like ammonium or sodium hydroxide as precipitants [33].

However, these synthesis methods present a challenge due to the long reaction times, which typically range from 4 to 48 h to produce nanoparticles smaller than 30 nm [34]. Therefore, developing more cost-effective methods to reduce reaction times, while preserving the characteristics of the nanoparticles required for their use as contrast agents, is essential.

Within the specialized literature, a reduction in synthesis times has been reported by administering large amounts of energy during the process, using direct ultrasounds [35]. Ultrasound generates cavitation effects that raise the temperature in specific areas of the synthesis, providing enormous amounts of energy and generating a much faster coprecipitation, reducing synthesis times to an average of 30 min [36]. However, this approach often results in high synthesis temperatures, which can destabilize the nanoparticles [37]. Therefore, it is necessary to develop a rapid synthesis method that avoids raising temperatures above 60 °C to obtain nanoparticles with the required properties.

In addition to the synthesis parameters, an important consideration when using Fe_3O_4 nanoparticles as contrast agents is their cytotoxicity on target tissues [38]. The toxicity of these nanoparticles has been reported due to the generation of free radicals caused by their susceptibility to oxidation, modifying the proper redox homeostasis of the target tissue and, consequently, altering the related metabolic pathways [39]. To address this issue,

the use of polymer coatings that can improve cell viability without greatly affecting the superparamagnetic properties of interest has been studied [40].

The (3-Aminopropyl) triethoxysilane (APTES) is a coating of great interest due to its high porosity, biocompatibility, and amino-terminal groups, which facilitate the formation of amide bonds with various molecules that can provide specificity to the nanoparticle. Therefore, using superparamagnetic nanoparticles coated with SiO_2-NH_2 and functionalized with biomarker molecules is a promising area of research for potential medical applications, where these nanoparticles could offer enhanced targeting capabilities [41].

In this context, the main objective of this work was to synthesize superparamagnetic Fe_3O_4 nanoparticles coated with SiO_2-NH_2 through ultrasonic-assisted chemical coprecipitation. The Fe_3O_4 nanoparticles were found to have a size of approximately 7.5 nm, with a SiO_2-NH_2 shell thickness of around 1 nm. The reduced synthesis time and costs allow a higher production rate of nanoparticles. Additionally, the Fe_3O_4@SiO_2-NH_2 nanoparticles were functionalized with the biomarker of neuroinflammation P-88, and their impact was evaluated on cell viability in an epithelial cell line. This approach offers a promising method for developing materials that allow to amplify the MRI signal detection, with potential medical applications and the ability to contribute to addressing global health challenges.

2. Results

2.1. Nanoparticle Characterization

2.1.1. X-Ray Diffraction (XRD)

Figure 1 displays the diffractogram of the Fe_3O_4 and Fe_3O_4@SiO_2-NH_2 nanoparticles, finding the characteristic peaks for the families of crystalline planes (111), (220), (311), (222), (400), (422), (511), (440), and (533) corresponding to a reverse spinel structure of magnetite (Fe_3O_4) (JCPDS card #75-0033 or COD#96-722-8111) [42]. Additionally, the diffractogram of the Fe3O4@SiO_2-NH_2 nanoparticle exhibits an appreciable broad peak between 20 and 30 degrees, confirming the presence of silica. The absence of a defined peak of SiO_2-NH_2 is due to the lack of crystallinity at the temperatures reached during the synthesis. When comparing the diffraction peaks of the samples, it is observed that they do not present any shift, revealing that the crystalline structure of the magnetite core remains unaltered, even after performing the SiO_2-NH_2 coating [43], the decrease in intensity in the peaks indicates the presence of the amorphous coating of SiO_2-NH_2 [44].

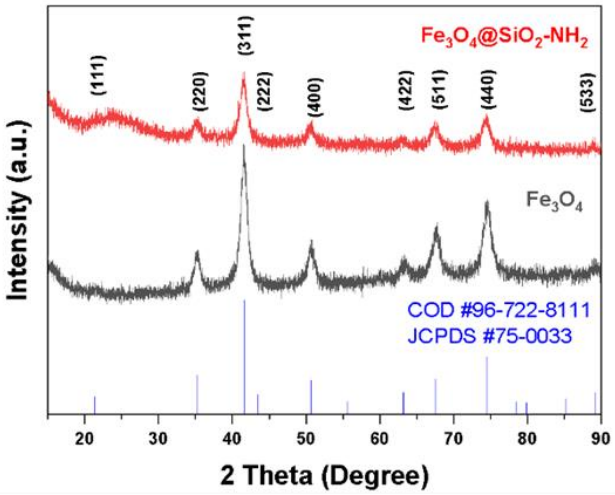

Figure 1. XRD of Fe_3O_4 nanoparticles (black) and SiO_2-NH_2-coated Fe_3O_4 nanoparticles (red).

The crystallite size was determined using the Scherrer equation. Average crystallite sizes of 7.43 nm and 7.83 nm for the bare Fe_3O_4 and Fe_3O_4@SiO_2-NH_2 nanoparticles, respectively, were determined (Table 1). The crystallite size of the bare Fe_3O_4 nanoparticles is close to the average size determined by TEM (cf. Section 2.1.6). As expected, this clearly

indicates that the Fe_3O_4 nanoparticles are single-domain nanoparticles [45], since for sizes smaller than 30 nm the formation of multiple domains is unfavorable energetically [46].

Table 1. Crystallite size of Fe_3O_4 and Fe_3O_4@SiO_2-NH_2 nanoparticles.

Sample	Theta (θ)	Beta (β)	K	Lambda (λ) (nm)	Crystallite Size (nm)	Mean Crystallite Size (nm)
Fe_3O_4	35.24	1.14	0.90	0.18	8.49	7.43
	41.58	1.09	0.90	0.18	9.08	
	50.68	1.54	0.90	0.18	6.65	
	63.31	2.58	0.90	0.18	4.20	
	67.62	1.43	0.90	0.18	7.79	
	74.58	1.39	0.90	0.18	8.37	
Fe_3O_4@SiO_2-NH_2	35.23	1.08	0.90	0.18	8.97	7.83
	41.58	1.18	0.90	0.18	8.40	
	50.68	1.51	0.90	0.18	6.75	
	63.30	1.58	0.90	0.18	6.84	
	67.59	1.42	0.90	0.18	7.80	
	74.55	1.41	0.90	0.18	8.21	

2.1.2. Fourier Transform Infrared Spectroscopy (FTIR)

Figure 2 shows the FTIR spectra for the bare Fe_3O_4 and SiO_2-NH_2-coated nanoparticles. In both cases, it is possible to observe the peak close to 540 cm^{-1} characteristics of the stretching of the Fe-O bonds, indicating the presence of iron oxide. In addition, the transmittance signals over 1000 cm^{-1} and 1500 cm^{-1} for the Fe_3O_4@SiO_2-NH_2 nanoparticles indicate the bending vibration of the Si-O bond [47] and bending of N-H bonds [48], respectively, specific to SiO_2-NH_2. The signals at 2920 cm^{-1} and 2850 cm^{-1} indicate stretching vibrations C-H. Finally, the band at 3400 cm^{-1} corresponds to the vibration of hydroxyl groups due to the O-H stretching model adsorbed on the surface of the Fe_3O_4 nanoparticles [49].

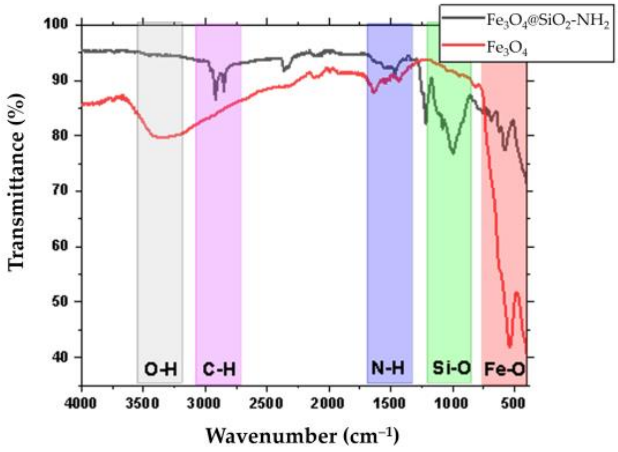

Figure 2. FITR of Fe_3O_4 and Fe_3O_4@SiO_2-NH_2 nanoparticles.

2.1.3. Differential Scanning Calorimetry-Thermogravimetric Analysis (DSC-TGA)

Figure 3 presents the decomposition of the nanoparticles as a function of temperature. Fe_3O_4 nanoparticles (Figure 3a) show a loss of up to 125 °C of 2% of the total weight due to the evaporation of the water present in the sample. Subsequently, a decomposition of the nanoparticle is observed progressively down to 92% when the temperature reaches 800 °C. This indicates the ability of nanoparticles to withstand high temperatures without evidencing a loss of total mass [50] and particularly at temperatures close to body temperature,

which is promising for medical applications [51]. Additionally, the ability to withstand high temperatures can propose nanoparticles as a possible helper in hyperthermia.

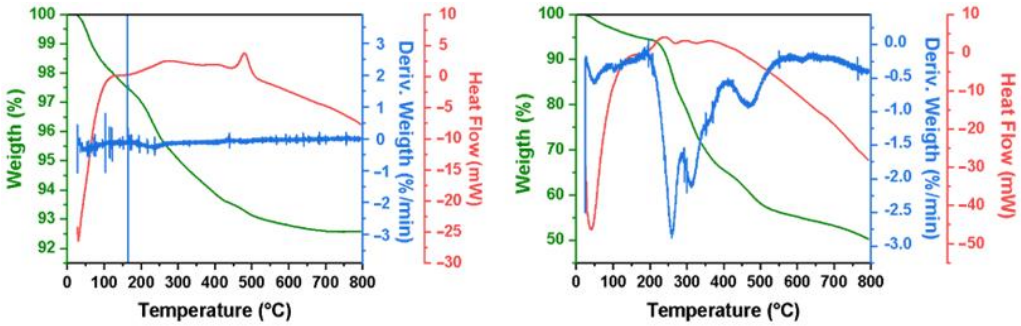

Figure 3. DSC-TGA of Fe_3O_4 (**a**) and (**b**) Fe_3O_4@SiO_2-NH_2 nanoparticles.

Figure 3a exhibits a constant decomposition of the nanoparticles without peaks that could indicate a large loss of mass at a specific temperature, as can be inferred from the derivative of weight per temperature [52]. In contrast, for Fe_3O_4 nanoparticles coated with SiO_2-NH_2 (Figure 3b), there is a loss of 6%wt of the sample when reaching 215 °C due to the evaporation of the different solvents and impurities. From 215 °C to 500 °C, the greatest loss occurs, reaching 57% of the initial weight of the Fe_3O_4@SiO_2-NH_2 nanoparticle, and at 800 °C, 50% of the initial mass is lost. The results evidenced the stability of the nanoparticles up to 215 °C [53]. The derivative of the weight with respect to temperature shows three degradation peaks, at 258 °C, 312 °C, and 468 °C, indicating the points of greatest total mass loss of the Fe_3O_4@SiO_2-NH_2 nanoparticle.

The DSC analysis for the Fe_3O_4 nanoparticles indicates the beginning of the structural transformation of the nanoparticles from magnetite (Fe_3O_4) to maghemite (γ-Fe_2O_3) at 136 °C. Likewise, the signal at 279 °C indicates the total transformation of nanoparticles to γ-Fe_2O_3 and, finally, the exothermic signal above 480 °C is attributed to the transformation of γ-Fe_2O_3 to hematite (α-Fe_2O_3) [54]. For the Fe_3O_4@SiO_2-NH_2 nanoparticle, there is a similar behavior: a first step from Fe_3O_4 to γ-Fe_2O_3, where the coating shifts the beginning of the transformation to 237 °C and the ending to 363 °C. Additionally, the transformation to α-Fe_2O_3 does not exist.

2.1.4. Vibrating Sample Magnetometry (VSM)

Figure 4 shows the temperature dependence (50 K < T < 400 K) of the magnetization in an applied field (H = 100 Oe) after a different cooling process in the ZFC and FC modes. The studies of magnetization as a function of temperature in ZFC and FC resulted in blocking temperatures of 187 K and 150 K for the uncoated and coated nanoparticles, respectively, and a maximum magnetization of 10.4 emu/g and 5.1 emu/g. These results demonstrate that both uncoated and coated NPs are superparamagnetic at room temperature and, more interestingly, at body temperature. Additionally, the magnetization as a function of the applied field was performed to determine the hysteresis loops, using a magnetic field range from −30 kOe to 30 kOe, while keeping the samples at room temperature. The magnetization values for the bare Fe_3O_4 nanoparticles are approximately 70 emu/g, while the coated Fe_3O_4@SiO_2-NH_2 nanoparticles exhibit a lower saturation magnetization of 27.5 emu/g (Figure S1). This decrease in magnetization is attributed to the presence of the SiO_2-NH_2 coating, which increases the overall mass of the nanoparticles. The specific magnetization of the coated sample was adjusted using a weight fraction of 0.75261 for Fe_3O_4, confirming that the sample contains pure Fe_3O_4 without significant transformation to maghemite. The extremely low coercive field of −0.078 Oe further supports the stability of Fe_3O_4 in the sample, indicating the absence of oxidation to maghemite. It is important to

note that, given the coercivity and remanence values are 0, the synthesized nanoparticles will exhibit superparamagnetic behavior at room temperature [55,56].

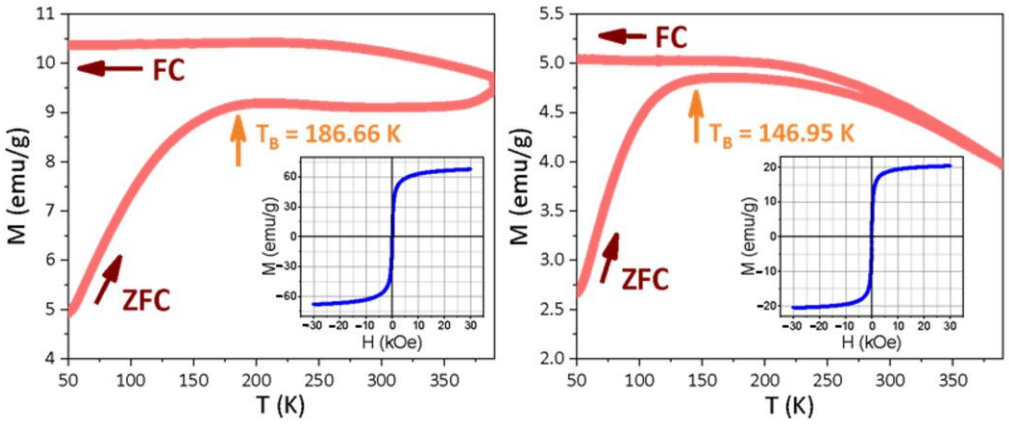

(**a**) (**b**)

Figure 4. Magnetic characterization curves of Fe_3O_4 (**a**) and (**b**) Fe_3O_4@SiO_2-NH_2 nanoparticles.

2.1.5. Scanning Electron Microscopy (SEM/EDX)

Figure S2 shows the surface morphology of the nanoparticles investigated by SEM. It can be observed a spherical and uniform morphology of Fe_3O_4 and Fe_3O_4@SiO_2-NH_2, necessary for the correct passage of those through biological barriers in medical application [57]. On the other hand, agglomeration is observed for the bare and coated nanoparticles due to the sample preparation process on the carbon tape [58]. A larger size is distinguished for nanoparticles with SiO_2-NH_2 coating (Figure S2b) [59], which suggests the formation of the coating on the nanoparticles; however, the size continues to be of great interest within the proposed application. However, the challenge is to achieve a greater dispersion [60].

Additionally, a surface chemical analysis was performed using EDX Figure S3, obtaining a semiquantitative composition of the elements present in the Fe_3O_4, Fe_3O_4@SiO_2-NH_2, and Fe_3O_4@SiO_2-NH_2/P-88 nanoparticles. Only iron (72%) and oxygen (28%) were detected for the Fe_3O_4 nanoparticles (Figure S3a), demonstrating that the synthesis method is adequate. On the other hand, the spectrum for the Fe_3O_4@SiO_2-NH_2 nanoparticle (Figure S3b) shows the presence of iron (37%), oxygen (42%), silicon (18%), and nitrogen (2%), indicating the presence of Fe_3O_4 nanoparticles, and the coating with SiO_2-NH_2 [61]. Finally, the spectrum of the functionalized nanoparticle (Fe_3O_4@SiO_2-NH_2/P-88) displays iron (8%), oxygen (26%), silica (12%), potassium (4%), chlorine (5%), sulfur (8%), sodium (5%), and carbon (26%), indicating the presence of Fe_3O_4 nanoparticles, a coating with SiO_2-NH_2, and the functionalization with P-88 due to carbon and sulfur from the carbon chain and methionine present in the peptide chain. The appearance of elements such as Cl, K, and Na is due to the resuspension in PBS of the sample (Figure S3c) [62].

2.1.6. High-Resolution Transmission Electron Microscopy (HR-TEM)

The morphology of the synthesized Fe_3O_4 nanoparticles, SiO_2-NH_2-coated Fe_3O_4 nanoparticles, and Fe_3O_4@SiO_2-NH_2/P-88 nanoparticles was analyzed using TEM (Figure 5). The bare Fe_3O_4 nanoparticles displayed a spherical morphology and a size of 7.61 $\pm$ 2.2 nm (Figure 5a) [63]. The coated Fe_3O_4 nanoparticles maintained the spherical morphology, and an increased size of 9.09 $\pm$ 1.77 nm is due to the presence of the coating with SiO_2-NH_2 (Figure 6b) [64]. Finally, the nanoparticle functionalized with P-88 also displayed a spherical morphology but a negligible increase in size (Figure 5c). These results agree with the results obtained by XRD (Figure 1). Indicating that the nanoparticle has the necessary morphological characteristics for its correct passage through the BBB [65] because it has a size of less than 50 nm (the necessary size for the correct absorption of nanoparticulate

materials) [66]. The inset of each image displays TEM images at a higher magnification. For the Fe_3O_4@SiO_2-NH_2 and Fe_3O_4@SiO_2-NH_2/P-88 nanoparticles, a dark internal structure and a lighter external layer are observed. Given that Fe_3O_4 has a higher density than SiO_2, this suggests the formation of a core@shell structure. This is confirmed by EDX analysis (Figure S4) conducted on the dark structures, which reveals that they are mostly composed of Fe and O. In contrast, the EDX of the outer layers shows an increase in Si. Additionally, the morphology of the nanoparticle influences the correct internalization of these in the target tissue, as the spherical shape is more appropriate compared to other structures for penetration in biological barriers, as has been reported elsewhere [65–68]. Finally, it has been reported that nanoparticles smaller than 20 nm could be digested and/or excreted by the body in two ways, by endocytosis of the same by cells and by elimination in feces and urine [69]. Avoiding adverse effects due to accumulation in the organs [70]. However, it should be noted that not only the size determines the form of elimination, but the charge and concentration of the nanoparticles also influence the correct movement of the latter through the body and, consequently its absorption and excretion. It is known that the low concentrations and neutral or positive charges of a nanoparticle do not affect the organism's integrity [71].

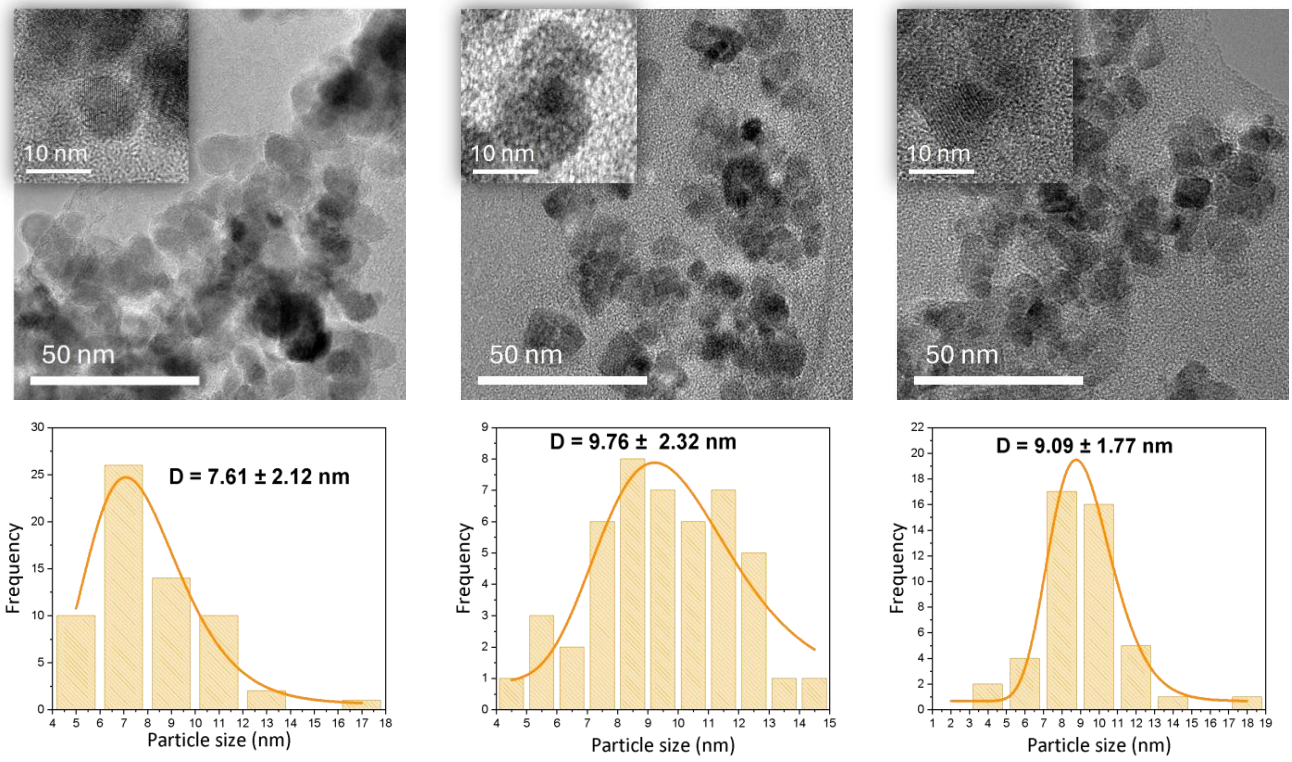

(**a**) (**b**) (**c**)

Figure 5. TEM of Fe_3O_4 (**a**), SiO_2-NH_2-coated Fe_3O_4 nanoparticles (**b**), and Fe_3O_4@SiO_2-NH_2/P-88 (**c**) nanoparticles, together with the corresponding nanoparticle size distributions.

The HRTEM analysis (Figure 6) allowed us to determine a structure like hexagons for the Fe_3O_4 nanoparticles. Additionally, the value of 0.301, corresponding to the interplanar distance of the family of crystalline planes (220), proper to said nanoparticles, is shown (Figure 6a). Confirmation of each of the crystalline planes reported in the diffractograms was performed using the fast Fourier transform Figure 6b. Table 2 records the presence of atomic distances corresponding to the crystalline planes (111), (220), (311), (222), (400), and (511) found in Figure 6b, which are specific to an inverse spinel structure of Fe_3O_4 (JCPDS Fe_3O_4 crystalline structure [72]. There are similarities indicating that the synthesized nanoparticles have an inverse spinel crystalline structure Figure 5c.

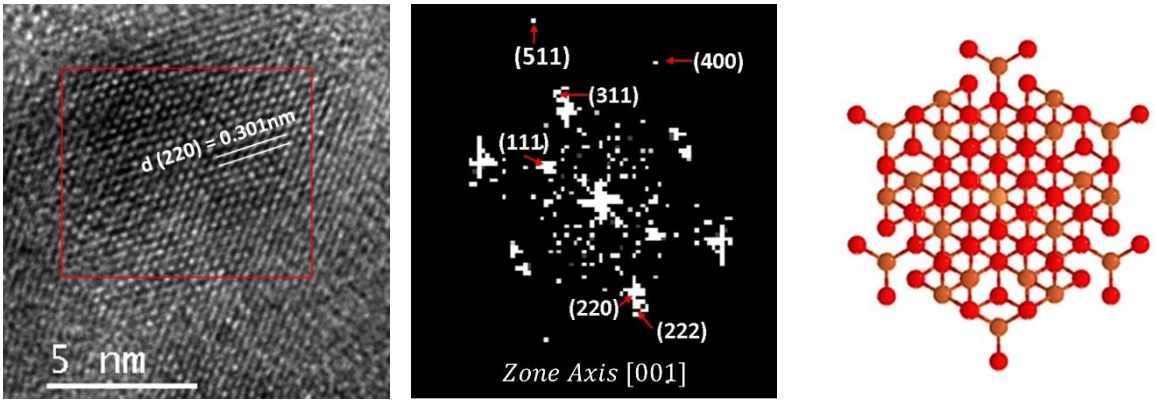

(**a**) (**b**) (**c**)

Figure 6. HRTEM of Fe_3O_4 nanoparticles (**a**), fast Fourier transform of Fe_3O_4 nanoparticles (**b**), and simulation of the crystalline structure of Fe_3O_4 nanoparticles verified through open access database The Materials Project (**c**).

Table 2. Fourier transform crystal planes determination.

Crystal Plane (hkl)	Theoretical Distance (nm)	Theoretical Value	Experimental Value	Experimental Distance (nm)
111	0.484	4.13	4.10	0.488
220	0.296	6.75	6.65	0.301
311	0.253	7.91	7.92	0.252
222	0.242	8.26	8.21	0.244
400	0.210	9.54	9.47	0.211
511	0.161	1.40	12.91	0.155

2.2. Peptide Anchoring on the Nanoparticle

The conjugation between the Fe_3O_4@SiO_2-NH_2 nanoparticle and the P-88 was evaluated using a biotin–streptavidin–HRP assay using the biotinylated peptide-88 for detection. The results reveal a 46% increase in absorbance for the nanoparticle functionalized with P-88 (Fe_3O_4@SiO_2-NH_2/P-88) compared to the nanoparticle without the peptide (Fe_3O_4@SiO_2-NH_2) (Figure 7a) (p = 0.033).

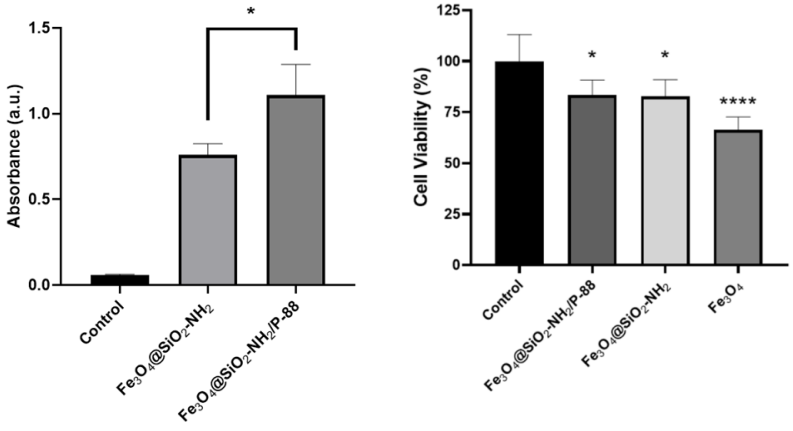

(**a**) (**b**)

Figure 7. (**a**) Verification of the anchorage of P-88 on the Fe_3O_4@SiO_2-NH_2 nanoparticle using a biotin-streptavidin-HRP assay (Student's test n:3 * $p < 0.05$). (**b**) Cell viability assays of Fe_3O_4, Fe_3O_4@SiO_2-NH_2, and Fe_3O_4@SiO_2-NH_2/P-88 nanoparticles (* $p < 0.05$, and **** $p < 0.0001$).

2.3. Cell Viability

The effects of Fe_3O_4, Fe_3O_4@SiO_2-NH_2, and Fe_3O_4@SiO_2-NH_2/P-88 nanoparticles on the viability of the Vero cell line were assessed using MTT assays (Figure 7b). The viability of cells exposed to bare nanoparticles was reduced by 33.8% ($p < 0.0001$ compared to the control), which can be attributed to the generation of reactive oxygen species (ROS) by the bare nanoparticles, leading to alterations in lipid metabolic pathways, cytokines, and cellular stress markers. Notably, the viability of cells exposed to coated nanoparticles showed a moderate decrease of 17.3% ($p = 0.0105$) for coated nanoparticles and 16.6% for functionalized coated nanoparticles ($p = 0.0129$) compared to the control. These results underscore the ability of the SiO_2-NH_2 coating, performed by ultrasonic cavitation to reduce the cytotoxicity of the superparamagnetic nanoparticles synthesized in the Vero cell line [73]. This finding opens the possibility of scaling up the study of functionalized nanoparticles for in vivo applications, particularly in MRI.

3. Discussion

Diffractogram analysis of Fe_3O_4 and Fe_3O_4@SiO_2-NH_2 nanoparticles confirms the spinel structure of magnetite; no changes in the diffraction peaks were observed, indicating that the core remains intact even after coating with SiO_2-NH_2. This suggests that the functionalization process does not alter the crystalline arrangement of magnetite. However, the decrease in peak intensity points to the amorphous nature of the silica coating. Moreover, the appearance of a broad peak between 20 and 30 degrees further validates the presence of silica in the coated nanoparticles. The crystallite size, determined using the Scherrer equation, closely aligns with the particle size measured by TEM, supporting the conclusion that these Fe_3O_4 nanoparticles are single domain. This is consistent with the nanoparticle size of less than 30 nm, as multi-domain formation becomes energetically unfavorable at this scale. Overall, the results highlight the successful synthesis of Fe_3O_4@SiO_2-NH_2 nanoparticles, preserving the magnetite core while introducing the amorphous silica shell. The coating of nanoparticles with SiO_2-NH_2 significantly alters their magnetic properties by reducing both the magnetization and blocking temperature, likely due to the increased mass of the coated particles. Despite this reduction, the superparamagnetic nature of the nanoparticles remains intact, even at room temperature, making them suitable for biomedical applications. The absence of coercivity and remanence in both coated and uncoated samples further reinforces their potential for use in environments where rapid magnetic response is crucial. The results indicate that conjugation between the Fe_3O_4@SiO_2-NH_2 nanoparticle and the peptide occurs effectively. This finding highlights the potential of conjugating diverse peptides that interact with molecular targets, conferring specificity to the nanoparticle to generate a contrast agent for MRI capable of detecting CNS diseases, even at early stages [37,73]. The BBB is a significant challenge in diagnosing and delivering therapies in the CNS; this hurdle can be overcome using nanoparticles with sizes <50 nm, as synthesized in this work. The superparamagnetic properties of Fe_3O_4 nanoparticles cause MRI signals to be more intense in the areas where they accumulate, allowing for better spatial resolution and precision in identifying lesions or abnormalities in the brain [74]. However, achieving nanoparticle functionalization is not the only objective in developing a nanomaterial as a contrast agent; it is also essential to evaluate its effects on cell biocompatibility to subsequently scale up to in vivo studies.

4. Materials and Methods

4.1. Synthesis of Fe_3O_4 Nanoparticles

For the synthesis of Fe_3O_4 nanoparticles, $FeCl_2 \cdot 4H_2O$ (ACS, Reag. Ph Eur) and $FeCl_3$*$6H_2O$ (ACS, Reag. Ph Eur) were dissolved in ultrapure water in a 250 mL three-necked vessel. Subsequently, a mixture of 100 mL of ultrapure water and 4 mL of 25% NH_3 (Reag. USP, Ph. Eur.) was added dropwise. All the above processes were performed using a Hielscher UP400ST ultrasonicator (400 W, 24 kHz), with a 14 mm diameter titanium sonic probe operating at a 90% pulse cycle and set to 60% ultrasonic maximum power (400 W).

The applied energy density was 310.5 J/mL. The maximum temperature of the process was 27 °C. Once dripping was complete, the nanoparticles were separated by magnetically assisted decantation and washed three times with ultrapure water.

4.1.1. Coating of Fe_3O_4 Nanoparticles with SiO_2-NH_2

The Fe_3O_4 nanoparticles were suspended in 100 mL of ultrapure water. Subsequently, SDS (PanReac Applichem) was incorporated into the nanoparticle suspension and APTES (Thermo Scientific) was added dropwise to coat the nanoparticles with a uniform SiO_2-NH_2 matrix. All the above processes were carried out using an ultrasonicator and the conditions described above. The maximum temperature of the process was 20 °C. After dripping, the nanoparticle was separated by magnetically assisted decantation and washed repeatedly. Finally, the nanoparticle was dried at 80 °C for 4 h in a forced convection drying oven, and the obtained powder was ground and stored in a dry place.

4.1.2. Functionalization of the Fe_3O_4@SiO_2-NH_2 Nanoparticle with the Biomarker P-88

An aliquot of 1.4 mg/mL concentration of Fe_3O_4@SiO_2-NH_2 was prepared in PBS at pH 5.7. From this aliquot, 100 µL was taken and mixed with 50 µL of PBS at pH 5.7 (Solution 1). On the other way, 1 mg of EDC and 1 mg of NHS were dissolved in 1 mL of PBS at pH 5.7 (Solution 2), later, 150 µL of Solution 2 was taken, and we added 1.6 µL of peptide 88. Both solutions were mixed and placed under orbital shaking for 12 h. The result was sterilized with UV light for 1 h and stored in a refrigerator at 2 °C.

An assay was carried out with a biotin–streptavidin–HRP system to identify the anchorage of the peptide P-88 in the Fe_3O_4@SiO_2-NH_2 nanoparticle. Starting from a 96-well plate, hydration with 1X PBS was performed overnight. Subsequently, the plate was washed three times with PBS/0.05% Tween-20 and blocked with 5% BSA/1X PBS (300 µL/well) for 2 h at room temperature. Again, the wells were washed 3 times. As a control, 100 µL of Fe_3O_4@SiO_2-NH_2 was used in one well, 100 µL of PBS was used as a blank, and 100 µL of Fe_3O_4@SiO_2-NH_2/P-88 was placed in another well. Each assay was performed in triplicate. Subsequently, the plate was washed 3 times and incubated with 100 µL streptavidin-HRP for 30 min at room temperature in the dark. Finally, the wells were washed 3 times, and 100 µL of the substrate (1:1, H_2O_2: tetramethylbenzidine, TMB) was added for 30 min at room temperature in the dark. The reaction was stopped with 1 M H_2SO_4 placed in 50 µL/well. The absorbance was determined at a wavelength of 450 nm in an FC Multiskan TM microplate reader.

4.2. Nanoparticle Characterization

4.2.1. Functionalization of the Fe_3O_4@SiO_2-NH_2 Nanoparticles with the Biomarker P-88

To obtain the X-ray diffraction pattern, a PANalytical brand X'PERT PRO MPD X-ray diffractometer with Cu-Kα radiation (λ = 0.154056 nm) was used. For the identification of the peaks and phases, the program X-Pert High Score plus version 3.0 of Panalytical was used. Samples of 30 mg of powdered Fe_3O_4 and Fe_3O_4@SiO_2-NH_2, previously dried and ground, were analyzed. The measurements were made with an angular step of 0.013° and an angular interval of 10° to 80° in 2θ. The Rietveld refinement technique was performed using Xpert Highscore plus software version 5.1.

4.2.2. Fourier Transform Infrared Spectroscopy (FTIR)

Infrared spectra were taken with a BRUKER ALPHA II FTIR unit with a range of 4000–400 cm^{-1} using 1% KBr pellets with 1 mg of Fe_3O_4 and Fe_3O_4@SiO_2-NH_2.

4.2.3. Vibrating Sample Magnetometry (VSM)

The thermogravimetric analysis with differential scanning calorimetry was carried out with SDT Q600 equipment from the Thermal Analysis brand, analyzing 10 °C/min from room temperature to 800 °C in a nitrogen atmosphere.

4.2.4. Thermogravimetric Analysis with Differential Scanning Calorimetry (DSC-TGA)

The magnetic characterization of the nanoparticles was carried out by the analysis of the magnetic hysteresis curves obtained by VSM. A Quantum Design magnetometer (VersaLab TM) was used at a temperature of 300 K with an applied field of −3T to 3T. The magnetization curves as a function of temperature in Field Cooled and Zero Field Cooled modes were also recorded. The studies of magnetization as a function of temperature were carried out following the magnetization routines of cooling without an applied magnetic field (Zero Field Cooling, ZFC) and cooling with an applied magnetic field (Field Cooling, FC), within a temperature interval from −223.15 °C to 126.85 °C.

4.2.5. Scanning Electron Microscopy (SEM/EDX)

A Teascan Lyra 3 model scanning electron microscope (SEM) was used with an energy disperse spectrometer (EDX) with excitation energies from 0.1 kV to 30 kV that produces high magnification images with high resolution (up to 3 nm). A sample of 30 mg of Fe_3O_4 and Fe_3O_4@SiO_2-NH_2 was used, suspended in water, and a carbon tape adhered to the metal sample holders as a substrate. These samples were dried in a vacuum.

4.3. Cell Viability

The VERO monkey renal epithelial cell line was grown in DMEM supplemented with 5% fetal bovine serum (FBS-GibcoTM). Cells were maintained in standard cell culture at conditions of 37 °C in a humidified atmosphere at 5% CO_2. The culture medium was replaced every 3 to 4 days, and when its influx exceeded 80% (2,000,000 and 8,000,000 cells for flaks of 25 and 75 cm^3, respectively), the corresponding passages were performed. Cells with a range of 17 passages were used for the MTT assays.

An MTT assay was performed to evaluate the cytotoxicity of the Fe_3O_4 nanoparticles, the Fe_3O_4@SiO_2-NH_2 nanoparticles, and the Fe_3O_4@SiO_2-NH_2/P-88 nanoparticles. From a 96-well plate, 20,000 cells were seeded per well, and the plate was allowed to incubate for 24 h. Subsequently, cells were evaluated with the following conditions: standard culture medium, DMSO 10%, Fe_3O_4, Fe_3O_4@SiO_2-NH_2, Fe_3O_4@SiO_2-NH_2/P-88, and Fe_3O_4@APTES without cells (Blank). After placing the stimuli, the plate was incubated for 24 h. After 24 h, 10 µL of MTT reagent was added, and the plate was incubated for 4 h. The medium was discarded and 100 µL of DMSO was added and the plate was allowed to incubate again for 20 min. The absorbance was determined at a wavelength of 570 nm in an FC Multiskan TM microplate reader. Each assay was performed in quintuplicate.

4.4. Statistical Analysis

Statistical analysis was performed using OriginPro® 2021b software and GraphPad Prism version 8.0.1. Differences between samples and control were assessed using Student's *t*-test. A value of $p < 0.05$ was considered statistically significant.

5. Conclusions

The synthesis of superparamagnetic Fe_3O_4 nanoparticles with a mean diameter of 7.61 nm with an inverse spinel structure and crystallite size of 7.43 nm and superparamagnetic properties was carried out at room temperature, in times less than 15 min, using coprecipitation assisted by ultrasound. With the use of sonochemistry, SiO_2-NH_2 coatings were obtained on the Fe_3O_4 nanoparticles, increasing their diameter to 9.09 nm while keeping the Fe_3O_4 core intact after coating. Additionally, the amorphous nature of the @SiO_2-NH_2 coating was confirmed, and, therefore, the decrease in the magnetic characteristics due to the shielding produced by the coating without affecting the superparamagnetic in the nanoparticle. The functionalization of the nanoparticle was verified by means of a biotin-streptavidin-HRP test, observing an increase in absorbance due to the presence of peptide-88 anchored on the nanoparticle. Finally, the effect of the Fe_3O_4 nanoparticles, the Fe_3O_4@SiO_2-NH_2 nanoparticles, and the Fe_3O_4@SiO_2-NH_2/P-88 nanoparticles on cell viability was determined, allowing us to propose these nanomaterials as a potential contrast

agent in magnetic resonance imaging to detect mild brain lesions, opening new alternatives in nanomedicine and early detection of brain diseases.

Supplementary Materials: The following supporting information can be downloaded at https://www.mdpi.com/article/10.3390/condmat9040049/s1, Figure S1: Magnetization curves at 300 K of Fe_3O_4@SiO_2-NH_2 during the reheating process. Figure S2: Representative SEM Images of the surface granularity of Fe_3O_4 (a) and (b) Fe_3O_4@SiO_2-NH_2 nanoparticles. Figure S3: EDX of Fe_3O_4 (a), Fe_3O_4@SiO_2-NH_2 nanoparticles (b) and Fe_3O_4@SiO_2-NH_2/P-88 nanoparticles (c). Figure S4: TEM image and EDX spectra with elemental composition in two zones of the nanoparticles: EDS-1 in the core and EDS-2 on the SiO_2-NH_2 coating.

Author Contributions: B.S.B.B.; methodology, formal analysis, data curation, I.M.S.G.; formal analysis, writing—original draft preparation, methodology, C.A.P.V.; supervision, investigation, writing—review and editing; K.V.-S., methodology, formal analysis; J.A.; methodology, validation, M.L.-B.; methodology, validation, J.R.; conceptualization, methodology, validation, D.L.P.; conceptualization, methodology, validation, writing—review and editing, all authors. All authors have read and agreed to the published version of the manuscript.

Funding: This research was funded by Universidad Antonio Nariño, grant number 2017223.

Data Availability Statement: This article contains the data used to support this study's conclusions.

Acknowledgments: We would like to express our gratitude to the Nanomaterials Laboratory of the Antonio Nariño University for providing us with the equipment and facilities necessary to carry out this research. We would like to acknowledge the support and valuable suggestions of Lidia Martínez and Yves Huttel from the Institute of Materials Science of Madrid (ICMM-CSIC).

Conflicts of Interest: The authors declare no conflicts of interest. The funders had no role in the design of this study; in the collection, analyses, or interpretation of data; in the writing of the manuscript; or in the decision to publish the results.

References

1. Segarra, M.; Aburto, M.R.; Acker-Palmer, A. Blood–Brain Barrier Dynamics to Maintain Brain Homeostasis. *Trends Neurosci.* **2021**, *44*, 393–405. [CrossRef]
2. Candelario-jalil, E.; Dijkhuizen, R.M.; Magnus, T. Neuroinflammation, Stroke, Blood-Brain Barrier Dysfunction, and Imaging Modalities. *Stroke* **2022**, *53*, 1473–1486. [CrossRef] [PubMed]
3. Peng, B.; Hao, S.; Tong, Z.; Bai, H.; Pan, S.; Lim, K.-L.; Li, L.; Voelcker, N.H.; Huang, W. Blood–brain barrier (BBB)-on-a-chip: A promising breakthrough in brain disease research. *Lab. Chip.* **2022**, *22*, 3579–3602. [CrossRef] [PubMed]
4. Zhao, Y.; Gan, L.; Ren, L.; Lin, Y.; Ma, C.; Lin, X. Factors influencing the blood-brain barrier permeability. *Brain Res.* **2022**, *1788*, 147937. [CrossRef] [PubMed]
5. Preininger, M.K.; Kaufer, D. Blood–Brain Barrier Dysfunction and Astrocyte Senescence as Reciprocal Drivers of Neuropathology in Aging. *Int. J. Mol. Sci.* **2022**, *23*, 6217. [CrossRef] [PubMed]
6. Segura-Collar, B.; Mata-Martínez, P.; Hernández-Laín, A.; Sánchez-Gómez, P.; Gargini, R. Blood-Brain Barrier Disruption: A Common Driver of Central Nervous System Diseases. *Neuroscientist* **2022**, *28*, 222–237. [CrossRef]
7. Piantino, M.; Kang, D.-H.; Furihata, T.; Nakatani, N.; Kitamura, K.; Shigemoto-Mogami, Y.; Sato, K.; Matsusaki, M. Development of a three-dimensional blood-brain barrier network with opening capillary structures for drug transport screening assays. *Mater. Today Bio* **2022**, *15*, 100324. [CrossRef]
8. Längrich, T.; Bork, K.; Horstkorte, R.; Weber, V.; Hofmann, B.; Fuszard, M.; Olzscha, H. Disturbance of Key Cellular Subproteomes upon Propofol Treatment Is Associated with Increased Permeability of the Blood-Brain Barrier. *Proteomes* **2022**, *10*, 28. [CrossRef]
9. Kadry, H.; Noorani, B.; Cucullo, L. A blood–brain barrier overview on structure, function, impairment, and biomarkers of integrity. *Fluids Barriers CNS* **2020**, *17*, 69. [CrossRef]
10. Pardridge, W.M. Blood–brain barrier endogenous transporters as therapeutic targets: A new model for small molecule CNS drug discovery. *Expert Opin. Ther. Targets* **2015**, *19*, 1059–1072. [CrossRef]
11. Blennow, K.; Hardy, J.; Zetterberg, H. The Neuropathology and Neurobiology of Traumatic Brain Injury. *Neuron* **2012**, *76*, 886–899. [CrossRef] [PubMed]
12. Visser, K.; Koggel, M.; Blaauw, J.; van der Horn, H.J.; Jacobs, B.; van der Naalt, J. Blood-based biomarkers of inflammation in mild traumatic brain injury: A systematic review. *Neurosci. Biobehav. Rev.* **2022**, *132*, 154–168. [CrossRef] [PubMed]
13. Sweeney, M.D.; Sagare, A.P.; Zlokovic, B.V. Blood–brain barrier breakdown in Alzheimer disease and other neurodegenerative disorders. *Nat. Rev. Neurol.* **2018**, *14*, 133–150. [CrossRef] [PubMed]
14. Thomas, I.; Dickens, A.M.; Posti, J.P.; Czeiter, E.; Duberg, D.; Sinioja, T.; Krakstrom, M.; Helmrich, I.R.A.R.; Wang, K.K.W.; Maas, A.I.R.; et al. Serum metabolome associated with severity of acute traumatic brain injury. *Nat. Commun.* **2022**, *13*, 2545. [CrossRef]

15. Lee, R.-L.; Funk, K.E. Imaging blood–brain barrier disruption in neuroinflammation and Alzheimer's disease. *Front. Aging Neurosci.* **2023**, *15*, 1144036. [CrossRef]
16. Kothari, S.F.; Eggertsen, P.P.; Frederiksen, O.V.; Thastum, M.M.; Svendsen, S.W.; Tuborgh, A.; Næss-Schmidt, E.T.; Rask, C.U.; Schröder, A.; Kasch, H.; et al. Characterization of persistent post-traumatic headache and management strategies in adolescents and young adults following mild traumatic brain injury. *Sci. Rep.* **2022**, *12*, 2209. [CrossRef]
17. van Gils, A.; Stone, J.; Welch, K.; Davidson, L.R.; Kerslake, D.; Caesar, D.; McWhirter, L.; Carson, A. Management of mild traumatic brain injury. *Pract. Neurol.* **2020**, *20*, 213–221. [CrossRef] [PubMed]
18. Lunkova, E.; Guberman, G.I.; Ptito, A.; Saluja, R.S. Noninvasive magnetic resonance imaging techniques in mild traumatic brain injury research and diagnosis. *Hum. Brain Mapp.* **2021**, *42*, 5477–5494. [CrossRef]
19. Ware, J.B.; Sinha, S.; Morrison, J.; Walter, A.E.; Gugger, J.J.; Schneider, A.L.; Dabrowski, C.; Zamore, H.; Wesley, L.; Magdamo, B.; et al. Dynamic contrast enhanced MRI for characterization of blood-brain-barrier dysfunction after traumatic brain injury. *NeuroImage Clin.* **2022**, *36*, 103236. [CrossRef]
20. Khairnar, S.; More, N.; Mounika, C.; Kapusetti, G. Advances in Contrast Agents for Contrast-Enhanced Magnetic Resonance Imaging. *J. Med. Imaging Radiat. Sci.* **2019**, *50*, 575–589. [CrossRef]
21. Lee, T.; Zhang, X.-A.; Dhar, S.; Faas, H.; Lippard, S.J.; Jasanoff, A. In Vivo Imaging with a Cell-Permeable Porphyrin-Based MRI Contrast Agent. *Chem. Biol.* **2010**, *17*, 665–673. [CrossRef] [PubMed]
22. Jenista, E.R.; Wendell, D.C.; Azevedo, C.F.; Klem, I.; Judd, R.M.; Kim, R.J.; Kim, H.W. Revisiting how we perform late gadolinium enhancement CMR: Insights gleaned over 25 years of clinical practice. *J. Cardiovasc. Magn. Reson.* **2023**, *25*, 18. [CrossRef] [PubMed]
23. Zhao, Z.; Li, M.; Zeng, J.; Huo, L.; Liu, K.; Wei, R.; Ni, K.; Gao, J. Recent advances in engineering iron oxide nanoparticles for effective magnetic resonance imaging. *Bioact. Mater.* **2022**, *12*, 214–245. [CrossRef] [PubMed]
24. Li, H.; Meade, T.J. Molecular Magnetic Resonance Imaging with Gd(III)-Based Contrast Agents: Challenges and Key Advances. *J. Am. Chem. Soc.* **2019**, *141*, 17025–17041. [CrossRef]
25. Felton, C.; Karmakar, A.; Gartia, Y.; Ramidi, P.; Biris, A.S.; Ghosh, A. Magnetic nanoparticles as contrast agents in biomedical imaging: Recent advances in iron- and manganese-based magnetic nanoparticles. *Drug Metab. Rev.* **2014**, *46*, 142–154. [CrossRef] [PubMed]
26. Jeon, M.; Halbert, M.V.; Stephen, Z.R.; Zhang, M. Iron Oxide Nanoparticles as T 1 Contrast Agents for Magnetic Resonance Imaging: Fundamentals, Challenges, Applications, and Prospectives. *Adv. Mater.* **2021**, *33*, e1906539. [CrossRef]
27. Liu, S.; Yu, B.; Wang, S.; Shen, Y.; Cong, H. Preparation, surface functionalization and application of Fe_3O_4 magnetic nanoparticles. *Adv. Colloid Interface Sci.* **2020**, *281*, 102165. [CrossRef]
28. Ullah Khan, A.; Chen, L.; Ge, G. Recent development for biomedical applications of magnetic nanoparticles. *Inorg. Chem. Commun.* **2021**, *134*, 108995. [CrossRef]
29. Ni, D.; Bu, W.; Ehlerding, E.B.; Cai, W.; Shi, J. Engineering of inorganic nanoparticles as magnetic resonance imaging contrast agents. *Chem. Soc. Rev.* **2017**, *46*, 7438–7468. [CrossRef]
30. Park, S.-M.; Aalipour, A.; Vermesh, O.; Yu, J.H.; Gambhir, S.S. Towards clinically translatable in vivo nanodiagnostics. *Nat. Rev. Mater.* **2017**, *2*, 17014. [CrossRef]
31. Hubert, V.; Dumot, C.; Ong, E.; Amaz, C.; Canet-Soulas, E.; Chauveau, F.; Wiart, M. MRI coupled with clinically-applicable iron oxide nanoparticles reveals choroid plexus involvement in a murine model of neuroinflammation. *Sci. Rep.* **2019**, *9*, 10046. [CrossRef] [PubMed]
32. Shen, Z.; Wu, A.; Chen, X. Iron Oxide Nanoparticle Based Contrast Agents for Magnetic Resonance Imaging. *Mol. Pharm.* **2017**, *14*, 1352–1364. [CrossRef] [PubMed]
33. Besenhard, M.O.; LaGrow, A.P.; Hodzic, A.; Kriechbaum, M.; Panariello, L.; Bais, G.; Loizou, K.; Damilos, S.; Cruz, M.M.; Thanh, N.T.K.; et al. Co-precipitation synthesis of stable iron oxide nanoparticles with NaOH: New insights and continuous production via flow chemistry. *Chem. Eng. J.* **2020**, *399*, 125740. [CrossRef]
34. Demin, A.M.; Pershina, A.G.; Minin, A.S.; Mekhaev, A.V.; Ivanov, V.V.; Lezhava, S.P.; Zakharova, A.A.; Byzov, I.V.; Uimin, M.A.; Krasnov, V.P.; et al. PMIDA-Modified Fe_3O_4 Magnetic Nanoparticles: Synthesis and Application for Liver MRI. *Langmuir* **2018**, *34*, 3449–3458. [CrossRef] [PubMed]
35. Barai, D.P.; Bhanvase, B.A. Production of Ag-doped Fe_3O_4 nanoparticles in ultrasound-assisted minireactor system. *Appl. Nanosci.* **2022**, *12*, 2889–2899. [CrossRef]
36. Braim, F.S.; Ab Razak, N.N.A.N.; Aziz, A.A.; Ismael, L.Q.; Sodipo, B.K. Ultrasound assisted chitosan coated iron oxide nanoparticles: Influence of ultrasonic irradiation on the crystallinity, stability, toxicity and magnetization of the functionalized nanoparticles. *Ultrason. Sonochem.* **2022**, *88*, 106072. [CrossRef]
37. Gahrouei, Z.E.; Imani, M.; Soltani, M.; Shafyei, A. Synthesis of iron oxide nanoparticles for hyperthermia application: Effect of ultrasonic irradiation assisted co-precipitation route. *Adv. Nat. Sci. Nanosci. Nanotechnol.* **2020**, *11*, 025001. [CrossRef]
38. Seyedjamali, T.; Farahzadi, M.K.; Arabi, H. Investigation of physical properties of Fe_3O_4/Au-Ag@MoS_2 nanoparticles on heat distribution in cancerous liver tissue. *Mater. Res. Express* **2022**, *9*, 095002. [CrossRef]
39. Vakili-Ghartavol, R.; Momtazi-Borojeni, A.A.; Vakili-Ghartavol, Z.; Aiyelabegan, H.T.; Jaafari, M.R.; Rezayat, S.M.; Bidgoli, S.A. Toxicity assessment of superparamagnetic iron oxide nanoparticles in different tissues. *Artif. Cells Nanomed. Biotechnol.* **2020**, *48*, 443–451. [CrossRef]

40. Fernández-Ramos, M.; Isasi, J.; Alcolea, M.; Munoz-Ortiz, T.; Ortiz-Rivero, E. New magnetic-fluorescent bifuntional ($Y_{0.9}Ln_{0.1}VO_4/Fe_3O_4$)@$SiO_2$ and [($Y_{0.9}Ln_{0.1}VO_4$@SiO_2)/Fe_3O_4@SiO_2] materials. *Ceram. Int.* **2022**, *48*, 22006–22017. [CrossRef]
41. Kadam, A.A.; Sung, J.S.; Sharma, B. Fe_3O_4-HNTs-APTES-palladium nanoparticles with enhanced high-temperature gas response properties. *J. Alloys Compd.* **2021**, *854*, 157041. [CrossRef]
42. Huang, J.-Y.; Chen, M.-H.; Kuo, W.-T.; Sun, Y.-J.; Lin, F.-H. The characterization and evaluation of cisplatin-loaded magnetite–hydroxyapatite nanoparticles (mHAp/CDDP) as dual treatment of hyperthermia and chemotherapy for lung cancer therapy. *Ceram. Int.* **2015**, *41*, 2399–2410. [CrossRef]
43. Khalid, A.; Ahmed, R.M.; Taha, M.; Soliman, T.S. Fe_3O_4 nanoparticles and Fe_3O_4@SiO_2 core-shell: Synthesize, structural, morphological, linear, and nonlinear optical properties. *J. Alloys Compd.* **2023**, *947*, 169639. [CrossRef]
44. Wei, Z.; Ma, X.; Zhang, Y.; Guo, Y.; Wang, W.; Jiang, Z.Y. High-efficiency adsorption of phenanthrene by Fe_3O_4-SiO_2-dimethoxydiphenylsilane nanoparticle: Experimental and theoretical study. *J. Hazard. Mater.* **2022**, *422*, 126948. [CrossRef] [PubMed]
45. Molaei, M.J.; Salimi, E. Magneto-fluorescent superparamagnetic Fe_3O_4@SiO_2@alginate/carbon quantum dots nanohybrid for drug delivery. *Mater. Chem. Phys.* **2022**, *288*, 126361. [CrossRef]
46. Maldonado-Camargo, L.; Unni, M.; Rinaldi, C. Magnetic Characterization of Iron Oxide Nanoparticles for Biomedical Applications. *Methods Mol. Biol.* **2017**, *1570*, 47–71.
47. Kulpa-Greszta, M.; Tomaszewska, A.; Michalicha, A.; Sikora, D.; Dziedzic, A.; Wojnarowska-Nowak, R.; Belcarz, A.; Pązik, R. Alternating magnetic field and NIR energy conversion on magneto-plasmonic Fe_3O_4@APTES–Ag heterostructures with SERS detection capability and antimicrobial activity. *RSC Adv.* **2022**, *12*, 27396–27410. [CrossRef] [PubMed]
48. Bondarenko, L.; Illés, E.; Tombácz, E.; Dzhardimalieva, G.; Golubeva, N.; Tushavina, O.; Adachi, Y.; Kydralieva, K. Fabrication, microstructure, and colloidal stability of humic acids loaded Fe_3O_4/aptes nanosorbents for environmental applications. *Nanomaterials* **2021**, *11*, 1418. [CrossRef]
49. Rashidi, S.; Iranmanesh, P.; Salarizadeh, P. Materials Science & Engineering C Fabrication, optimization, and characterization of ultra-small superparamagnetic Fe_3O_4 and biocompatible Fe_3O_4@ZnS core/shell magnetic nanoparticles: Ready for biomedicine applications. *Mater. Sci. Eng. C* **2019**, *98*, 205–212.
50. Pekdemir, M.E.; Aydin, D.; Pekdemir, S.S.; Sönmez, P.E.; Aksoy, E. Shape Memory Polymer-Based Nanocomposites Magnetically Enhanced with Fe_3O_4 Nanoparticles. *J. Inorg. Organomet. Polym. Mater.* **2023**, *33*, 1147–1155. [CrossRef]
51. Fekri, L.Z.; Zadeh, L.H. Copper/dapsone cuvalented Fe_3O_4@SiO_2-propyl nanoparticle as a highly active and magnetically recoverable Lewis acid catalyst for the novel synthesis of bis-dapsone derived acridines. *J. Chin. Chem. Soc.* **2021**, *68*, 1673–1685. [CrossRef]
52. Karimzadeh, I.; Aghazadeh, M.; Ganjali, M.R.; Doroudi, T.; Kolivand, P.H. Preparation and characterization of iron oxide (Fe_3O_4) nanoparticles coated with polyvinylpyrrolidone/polyethylenimine through a facile one-pot deposition route. *J. Magn. Magn. Mater.* **2017**, *433*, 148–154. [CrossRef]
53. Huang, Y.; Wang, Y.; Wang, Y.; Pan, Q.; Ding, X.; Xu, K.; Li, N.; Wen, Q. Ionic liquid-coated Fe_3O_4/APTES/graphene oxide nanoparticles: Synthesis, characterization and evaluation in protein extraction processes. *RSC Adv.* **2016**, *6*, 5718–5728. [CrossRef]
54. Yuan, P.; Fan, M.; Yang, D.; He, H.; Liu, D.; Yuan, A.; Zhu, J.; Chen, T. Montmorillonite-supported magnetite nanoparticles for the removal of hexavalent chromium [Cr(VI)] from aqueous solutions. *J. Hazard. Mater.* **2009**, *166*, 821–829. [CrossRef] [PubMed]
55. Mostafaei, M.; Hosseini, S.N.; Khatami, M.; Javidanbardan, A.; Sepahy, A.A.; Asadi, E. Isolation of recombinant Hepatitis B surface antigen with antibody-conjugated superparamagnetic Fe_3O_4/SiO_2 core-shell nanoparticles. *Protein Expr. Purif.* **2018**, *145*, 1–6. [CrossRef] [PubMed]
56. Yin, N.; Wang, X.; Yang, T.; Ding, Y.; Li, L.; Zhao, S.; Li, P.; Xu, X.; Zhu, L. Multifunctional Fe_3O_4 cluster @ quantum dot-embedded mesoporous SiO_2 nanoplatform probe for cancer cell fluorescence-labelling detection and photothermal therapy. *Ceram. Int.* **2021**, *47*, 8271–8278. [CrossRef]
57. Marzieh, A.N.; Deinavizadeh, M.; Kiasat, A.R. Fe_3O_4@SiO_2/DABCO(OH) Core-Shell Hybrid Nanoparticle: Efficient Nanomagnetic and Basic Reusable Catalyst in the One-pot Synthesis of Trithiocarbonate Derivatives. *Mater. Chem. Horizons* **2023**, *2*, 81–92.
58. Prabu, D.; Kumar, P.S.; Indraganti, S.; Sathish, S.; Kumar, J.A.; Anand, K.V. One-Step Fabrication of Amino-Functionalized Fe_3O_4@SiO_2 Core-Shell Magnetic Nanoparticles as a Potential Novel Platform for Removal of Cadmium (II) from Aqueous Solution. *Sustainability* **2022**, *14*, 2290. [CrossRef]
59. Nikpassand, M.; Keyhani, A.; Fekri, L.Z.; Varma, R.S. Mechanochemical synthesis of azo-linked 2-amino-4H-chromene derivatives using Fe_3O_4@SiO_2@KIT-6-NH2@Schiff-base complex nanoparticles. *J. Mol. Struct.* **2022**, *1251*, 132065. [CrossRef]
60. Zhu, Q.; Song, J.; Liu, Z.; Wu, K.; Li, X.; Chen, Z.; Pang, H. Photothermal catalytic degradation of textile dyes by laccase immobilized on Fe_3O_4@SiO_2 nanoparticles. *J. Colloid Interface Sci.* **2022**, *623*, 992–1001. [CrossRef]
61. Rezayati, S.; Kalantari, F.; Ramazani, A. Picolylamine-Ni(ii) complex attached on 1,3,5-triazine-immobilized silica-coated Fe_3O_4 core/shell magnetic nanoparticles as an environmentally friendly and recyclable catalyst for the one-pot synthesis of substituted pyridine derivatives. *RSC Adv.* **2023**, *13*, 12869–12888. [CrossRef]
62. Mofatehnia, P.; Ziarani, G.M.; Elhamifar, D. A new yolk-shell hollow mesoporous nanocomposite, Fe_3O_4@SiO_2@MCM41-IL/WO_4^{2-}, as a catalyst in the synthesis of novel pyrazole coumarin compounds. *J. Phys. Chem. Solids* **2021**, *155*, 110097. [CrossRef]

63. Tarighat, M.A.; Ghorghosheh, F.H.; Abdi, G. Fe_3O_4@SiO_2-Ag nanocomposite colorimetric sensor for determination of arginine and ascorbic acid based on synthesized small size AgNPs by cystoseria algae extract. *Mater. Sci. Eng. B* **2022**, *283*, 115855. [CrossRef]
64. Purwiandono, G.; Fatimah, I.; Sahroni, I.; Citradewi, P.W.; Kamari, A.; Sagadevan, S.; Oh, W.-C.; Doong, R.-A. Fe_3O_4@SiO_2 nanoflakes synthesized using biogenic silica from *Salacca zalacca* leaf ash and the mechanistic insight into adsorption and photocatalytic wet peroxidation of dye. *Green Process. Synth.* **2022**, *11*, 345–360. [CrossRef]
65. Verma, A.; Stellacci, F. Effect of surface properties on nanoparticle-cell interactions. *Small* **2010**, *6*, 12–21. [CrossRef]
66. Sonavane, G.; Tomoda, K.; Makino, K. Biodistribution of colloidal gold nanoparticles after intravenous administration: Effect of particle size. *Colloids Surfaces B Biointerfaces* **2008**, *66*, 274–280. [CrossRef] [PubMed]
67. Liu, H.-J.; Xu, P. Strategies to overcome/penetrate the BBB for systemic nanoparticle delivery to the brain/brain tumor. *Adv. Drug Deliv. Rev.* **2022**, *191*, 114619. [CrossRef]
68. Meola, A.; Rao, J.; Chaudhary, N.; Sharma, M.; Chang, S.D. Gold nanoparticles for brain tumor imaging: A systematic review. *Front. Neurol.* **2018**, *9*, 328. [CrossRef]
69. Patil, R.M.; Shete, P.B. *Biodistribution and Cellular Interaction of Hybrid Nanostructures*; Elsevier Inc.: Amsterdam, The Netherlands, 2019.
70. Jo, D.H.; Kim, J.H.; Lee, T.G.; Kim, J.H. Size, surface charge, and shape determine therapeutic effects of nanoparticles on brain and retinal diseases. *Nanomed. Nanotechnol. Biol. Med.* **2015**, *11*, 1603–1611. [CrossRef]
71. Ghosh, D.; Upmanyu, N.; Shukla, T.; Shrivastava, T.P. *Cell and Organ Drug Targeting*; Elsevier Inc.: Amsterdam, The Netherlands, 2019.
72. Petousis, I.; Mrdjenovich, D.; Ballouz, E.; Liu, M.; Winston, D.; Chen, W.; Graf, T.; Schladt, T.D.; Persson, K.A.; Prinz, F.B. Data Descriptor: High-throughput screening of inorganic compounds for the discovery of novel dielectric and optical materials. *Sci. Data* **2017**, *4*, 160134. [CrossRef]
73. Wu, M.; Li, X.; Guo, Q.; Li, J.; Xu, G.; Li, G.; Wang, J.; Zhang, X. Magnetic mesoporous silica nanoparticles-aided dual MR/NIRF imaging to identify macrophage enrichment in atherosclerotic plaques. *Nanomed. Nanotechnol. Biol. Med.* **2021**, *32*, 102330. [CrossRef] [PubMed]
74. Rahman, M. Magnetic Resonance Imaging and Iron-oxide Nanoparticles in the era of Personalized Medicine. *Nanotheranostics* **2023**, *7*, 424–449. [CrossRef] [PubMed]